ARCHIVES OF MECHANICS
Arch. Mech. **77** (6), 573–593, 2025, https://doi.org/10.24423/aom.4688

Simulation of transient fluid–structure interaction in flapping-wing micro aerial vehicles

W. STANKIEWICZ[1*)], T. KRAKOWSKI[1)], K. FOLTYŃSKI[2)]

[1)] *Division of Virtual Engineering, Institute of Applied Mechanics, Poznan University of Technology, Jana Pawla II 24, 60-965 Poznan, Poland, e-mail*[*)] *: witold.stankiewicz@put.poznan.pl*

[2)] *Faculty of Mechanical Engineering, Poznan University of Technology, Piotrowo 3, 60-965 Poznan, Poland*

The objective of this study is to investigate aeroelastic phenomena occurring during airflow around flapping wings of a micro aerial vehicle (MAV) inspired by insect anatomy. A numerical model of the wing and the flow configuration was developed based on an experiment conducted at ESPCI Paris. Transient fluid–structure interaction (FSI) simulations were carried out in the Ansys environment, employing independent solvers for fluid flow (CFD) and structural deformation (FEM), coupled through the System Coupling module. The analysis focused on the role of wing compliance in thrust generation, with particular attention to the effects of flapping frequency and wing stiffness, determined by the thickness of the membrane forming the lifting surface. The results demonstrate a strong dependence of thrust generation on the degree of wing deformation, in good agreement with the experimental findings. These findings highlight the importance of structural flexibility in enhancing aerodynamic performance and provide practical guidelines for the design of efficient flapping-wing micro aerial vehicles.

Key words: fluid–structure interactions, FSI, aeroelasticity, CFD, MAV, microdrone, bio-inspired, flapping wings.

1. Introduction

Lightweight, unmanned aerial vehicles (UAVs), also known as drones, can serve both civilian and military applications as mobile systems for gathering information in hard-to-reach and hazardous areas. Examples of their possible applications include post-earthquake reconnaissance to locate survivors or assess damage in collapsed structures, exploration of caves, mines, or underground tunnels, as well as surveying dangerous terrain, such as active landslides, unstable cliffs or volcanoes, in order to conduct scientific research and

The preliminary results of this study were presented at the TKI'2024 conference.

environmental monitoring. The unmanned vehicles might facilitate such important tasks, as surveillance of infrastructure, such as power lines, pipelines and bridges, especially in difficult-to-access locations. The ability of small UAVs to operate in confined spaces, like inside buildings or over rough terrain, has been shown to be useful in gathering intelligence in situations where larger UAVs or human teams cannot go.

In this context, the potential miniaturization of such vehicles is of great importance, often reducing their dimensions to just a few centimeters and their weight to mere tens of grams [1]. At this scale, traditional solutions typical of conventional airplanes or multirotors may prove ineffective. Drawing inspiration from nature leads to bionic models based on insects, where lift and thrust are generated simultaneously through wing flapping, with the deformation of flexible wings playing a crucial role in this process.

One of the examples of such devices is the OVMI drone, weighing 20 mg with a wingspan of approximately 22 mm, developed by S. Grondel's team at the IEMN institute in Valenciennes and Lille, France [2]. Its wings are composed of a 3D skeleton made from multiple layers of SU-8 photoresist, with thicknesses ranging between 40 μm and 150 μm, and the membranes made of a 400 nm thick film of Parylene C. This drone utilizes resonant vibrations, generated by a single electromagnetic actuator, to amplify the wing flapping and twisting amplitudes. These motions are in quadrature phase shift, achieved by designing the geometry to minimize the frequency gap between the two resonant modes. The resulting design generates enough lift force to overcome the prototype's weight.

Another example is a 60 mg drone with a wingspan of 3 cm, designed by R.J. Wood at Harvard University [3]. The wings are made of carbon-fiber 'veins' and a membrane from a polymer face sheet 1.5 μm thick. It is powered by a single piezoelectric bending cantilever microactuator, weighing 40 mg. It generates flapping resonance near 110 Hz and rotational resonance close to 250 Hz, which results in a wing trajectory nearly identical to biological counterparts. The presented prototype is able to take off with an external power supply.

Another notable design is DelFly II, developed by the team from Delft University [4]. This biplane-wing vehicle weighs 16 g and has a wingspan of 28 cm. Each wing consists of a carbon-rod leading-edge spar, a thin Mylar foil, and two stiffeners. The leading-edge spar is actively driven by a brushless motor, while the foil deforms passively. The flapping frequency of 13 Hz has been proven to be sufficient to support hovering flight of the prototype having a pressure sensor and a microcontroller onboard.

Finally, B. Thiria and R. Godoy-Diana at ESPCI Paris [5] experimentally studied a self-propelled flapping-wing flyer mounted on a circular track ('merry-go-round') to analyze the effects of wing compliance on propulsion efficiency. The wings, with a span of approximately 150 mm and modeled as flexible plates,

were driven by a mechanical system that simulated sinusoidal motion. This study served as a basis for this work within a virtual environment, and it is presented in more detail in the following section of this paper.

All of the aforementioned bio-inspired micro aerial vehicles (MAVs) have similar goals: to provide maneuverability (including hovering) and small size that allow them to operate in confined environments, as well as to propose propulsive efficiency, taking advantage of aerodynamic phenomena often omitted in traditional fixed-wing or multirotor approaches. The examples are the formation of a leading-edge vortex (LEV), which generates a pressure drop and increases the lift and 'clap and fling' phenomenon, where the wings of some insects (such as mosquitoes or small flies) come together at the peak of the stroke (clap), and then they rapidly separate (fling), creating strong vortices that enhance the lift [6].

The motivation for enhancing the fidelity of CFD simulations for the MAV design is the need for high-quality data to support AI-enhanced methods. For example, Kawakami *et al.* [7] used computational FSI to study flapping, flexible wings bio-inspired MAV configurations considered promising for Mars exploration – which provide valuable reference data when combining data driven surrogates with validated physics-based simulations. Another example is the work of Gupta *et al.* [8], who utilized FSI modeling for a morphing-wing drone (Aerobat) not only for design purposes but also for developing a control strategy that integrates unsteady aerodynamic FSI models with trajectory tracking control. More recent studies by Drikakis *et al.* [9] demonstrate the use of transformer architectures to predict FSI responses in high-speed transients involving shocks and turbulent layers. Such sequence models can be adapted to predict time-series aeroelastic states for rapid flight-envelope assessment, including for flapping-wing drones. Finally, the potential of non-intrusive, physics-aware ML predictors – such as the encoder regressor decoder reduced order models to provide improved initial guesses for partitioned FSI timesteps and accelerate convergence in strongly coupled problems is highlighted in the work of Tiba *et al.* [10].

Despite the progress in the MAV design, there remains a clear gap in understanding how wing compliance and flapping parameters interact to influence thrust generation and aerodynamic efficiency in bio-inspired flapping-wing systems. While experimental studies, such as those by Thiria and Godoy-Diana, provide valuable observations, numerical modeling that captures the coupled fluid-structure interactions under varying wing stiffness and flapping frequency is still limited.

The objective of this study is to address this gap by performing transient numerical simulations of flapping wings, with the aim of quantifying the effects of wing configuration on thrust and aerodynamic performance, and providing insights that can inform the design of efficient bio-inspired MAVs.

2. Research object and setup

The experimental setup by B. Thiria and R. Godoy-Diana [5, 11] consisted of a pair of flexible wings mounted at the end of a rod with a length of $R = 0.5\,\mathrm{m}$, which in turn was ball-bearing mounted to a central shaft. The wings were composed of polyvinyl chloride membranes in the shape of semicircles with a diameter of $d = 60\,\mathrm{mm}$, attached to the leading edge, that was rigidified by a fiberglass structure. Their thickness ranged from 0.15 mm to 0.4 mm, depending on the configuration, which resulted in bending rigidities in the range typical to many real-life insects [12].

The wing system was driven by an electric motor mounted on the rod, which, through the gear mechanism and linkage system, set the leading edges into motion. The flapping motion of the wings generated thrust, causing rotational motion of the entire system around the shaft.

The experimental setup is shown in Fig. 1. The thrust was measured using a calibrated weight attached via a string passed through a pulley, which held the system in a fixed position during flapping, while the weight deficit was monitored on a tabletop balance.

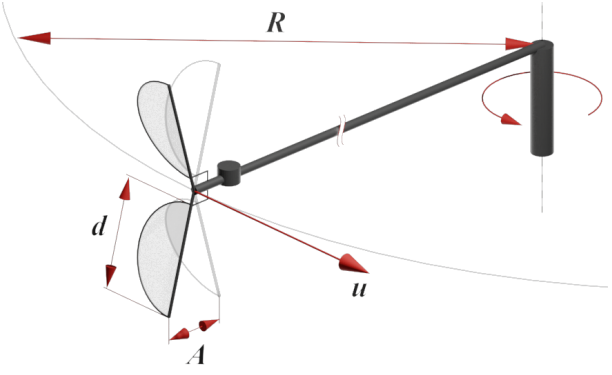

Fig. 1. The drone model from the experiment [5], which serves as the basis for the analyzed configuration, showing key dimensions and velocity: R – rod length, d – wing diameter, A – wing tip amplitude, $\mathbf{u}$ – velocity vector.

In the experiment, the flapping motion of the wings was characterized by the peak-to-peak amplitude at the spanwise position of the maximum chord, set to 30 mm, which corresponded to an amplitude of $A = 50\,\mathrm{mm}$ at the wing tip.

In this study, the experiment is reproduced numerically in order to systematically analyze the influence of wing compliance and flapping parameters on thrust generation, which cannot be easily varied in the physical setup. In the

numerical simulations the oscillatory motion was induced at the leading edge with an amplitude of $\phi_0 = 38.94°$, reproducing the wing motion observed in the experiment.

For the analysis, a single flapping wing was considered, assuming symmetry across the entire system. The symmetry assumption is valid in the present study because only propulsion effects are considered, and the actuator configuration permits exclusively symmetric operation. However, for future investigations focused on flight-control dynamics, this assumption would no longer be appropriate. The wing oscillated around a fixed point at frequencies ranging from 10 to 30 Hz. The wings were modeled as flexible membranes made of polyvinyl chloride (density $\rho = 1400\,\mathrm{kg/m^3}$, Poisson's ratio $\nu = 0.4$) with rigid (non-deformable) leading edges, where boundary conditions for oscillation were applied. Young's modulus was adjusted (in the range 3.9–5.7 GPa) so that the natural vibration frequencies of the wings for each membrane thickness match the values described in the experiment. Thus, the influence of the fiberglass structure (with unknown parameters) rigidifying the leading edge was approximated by adjusting the material properties of the membrane.

The first three natural frequencies, obtained from the finite element analysis, are listed in Table 1, with the corresponding free vibration mode shapes shown in Fig. 2. They (the modes) represent, respectively: the bending of the membrane about the y-axis, which coincides with the leading edge; the twisting of the membrane about the x-axis, aligned with the thrust force direction; and edgewise bending of the trailing edge in the z-direction.

TABLE 1. Natural frequencies for membranes of different thickness.

Thickness [mm]	f_1 [Hz] (bending)	f_2 [Hz] (twisting)	f_3 [Hz] (edgewise bending)
0.15	70.80	142.16	261.02
0.23	111.23	223.31	409.98
0.25	125.43	251.79	462.25
0.40	166.69	334.51	613.91

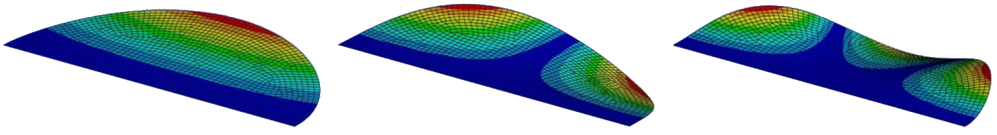

FIG. 2. The first three vibration mode shapes for the analyzed configuration, corresponding to the natural frequencies f_1 (bending), f_2 (twisting), and f_3 (edgewise bending) from Table 1. Membrane is oscillating around the (rigid) leading edge aligned with the y-axis.

The oscillatory motion was applied at the leading edge of the wing, according to the formula:

$$\boldsymbol{\phi}(t) = \phi_0 \sin(2\pi f t)\, \hat{\mathbf{x}} \tag{2.1}$$

(where $\hat{\mathbf{x}}$ is the unit vector along the X-axis), leading to the heaving of the wing. Meanwhile, the elastic material of the membrane allows for passive pitching of the wing around its transverse axis [11]. Together, these motions define the flapping movement, affecting generation of the thrust.

The heaving occurs around the X-axis, along which thrust is measured. Based on the experiment [5], it was assumed that the Y-axis corresponds to the direction of gravity (neglected here). Therefore, the forces measured along this axis correspond to lift. It should be noted that the second wing (omitted here due to the assumption of symmetry) would generate a force acting in the opposite direction. The force acting along the Z-axis averages out to zero for each wing within every cycle.

3. Methodology

The analysis of aeroelastic phenomena occurring during wing flapping was conducted using loosely-coupled fluid-structure interaction (FSI) system consisting of two separate solvers, each operating on separately generated computational grids discretizing fluid and solid domains, respectively.

Ansys Fluent was employed to calculate velocity and pressure fields in the flow, particularly along the boundary of the computational domain (wing surface). The governing equations for compressible flow incorporated the motion of the flow mesh resulting from structural deformations.

This approach, known as the Arbitrary Lagrangian–Eulerian (ALE) method [13–15], results in equations of the form:

$$\frac{\partial}{\partial t}(\boldsymbol{\rho u}) + \nabla \cdot \big(\boldsymbol{\rho}(\boldsymbol{u} - \boldsymbol{u}_{grid}) \otimes \boldsymbol{u}\big) + \nabla \boldsymbol{p} - \nabla \cdot \boldsymbol{\tau} = 0, \tag{3.1}$$

where $\boldsymbol{u}$, $\boldsymbol{p}$ and $\boldsymbol{\rho}$ are velocity, pressure and density fields, respectively. The diffusive term describes the divergence of the stress tensor $\boldsymbol{\tau}$, and the convective term involves $\boldsymbol{u} - \boldsymbol{u}_{grid}$ which represents the relative velocity between the material and the mesh, referred to as the convective velocity [14].

In Eq. (3.1), $\boldsymbol{u}_{grid}$ denotes the mesh velocity field, which arises from the motion/deformation of the computational domain and appears only in the convective term. The tensor $\boldsymbol{\tau}$ corresponds to the viscous (deviatoric) stress tensor, defined as:

$$\boldsymbol{\tau} = \mu \left(\nabla \boldsymbol{u} + (\nabla \boldsymbol{u})^T\right) - \frac{2}{3}\mu(\nabla \cdot \boldsymbol{u})\boldsymbol{I}, \tag{3.2}$$

for a Newtonian, compressible fluid, where μ is the dynamic viscosity and $\boldsymbol{I}$ is the identity tensor.

The fluid flow model consisted of RANS equations closed with the three-equation transition k-k_L-ω turbulence model by D.K. WALTERS and D. COKLJAT [16], which belongs to the family of k-ω turbulence models originally proposed by D.C. WILCOX [17]. The selected k-k_L-ω model extends the classical k-ω approach by including an additional transport equation for laminar kinetic energy. It proved to be useful in modeling flow past flat planes and airfoils in laminar-to-turbulent transition, occurring at low-to-moderate Reynolds numbers.

The deformation of the wing structure was analyzed using Ansys Mechanical, applying Hooke's law to model the linear elastic stress-strain behavior of the isotropic membrane material (PVC).

Meshes used by both codes are non-conforming – in terms of formulation (finite elements for the solid domain and finite volumes for the fluid domain), element types and order, as well as the level of discretization, which creates the need of coupling of these solvers.

The entire coupling process, described in detail in the paper on the Ansys Workbench *Coupling* module [18], is briefly presented in Fig. 3. The pressures calculated in the flow field are extracted from the boundary of the wing and transferred as aerodynamic forces to the computational structural mechanics (CSM) model using interpolation tools [13, 15, 19, 20]. Subsequently, a finite

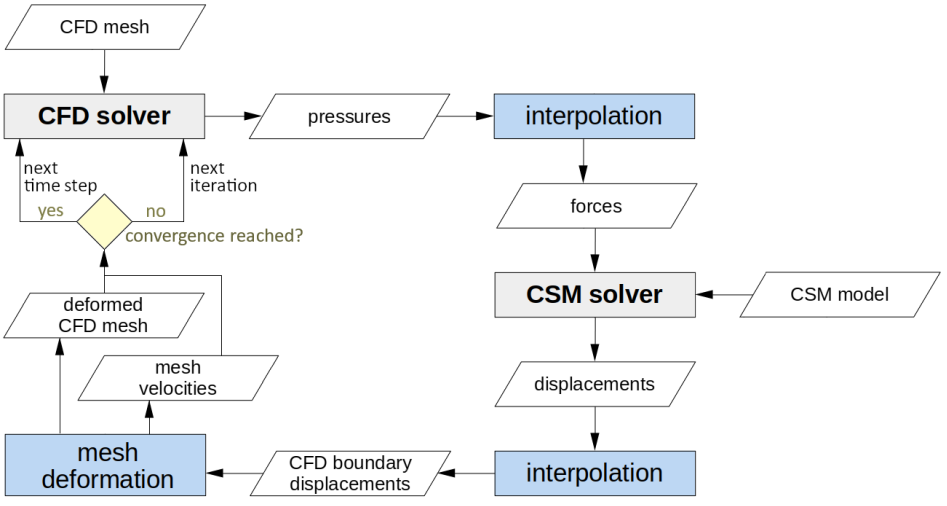

FIG. 3. Block diagram of the aeroelastic simulations workflow, showing the iterative coupling between the CFD and CSM solvers within each time step, followed by advancement to the next step. Pressure loads and structural displacements are exchanged through interpolation, and mesh deformation updates the CFD domain accordingly.

element-based solver is used to obtain the displacements of the mesh representing the wing's structure, as well as the stress distribution. Once again, interpolation tools are employed to transfer the nodal displacements from the CSM model to the boundary of the CFD mesh. Subsequently, deformation tools, such as those based on spring analogy [15, 19] or radial basis functions (RBF) [21], are applied to deform the CFD mesh according to the displacements at the wing boundary. As a result, a deformed mesh and the grid velocity field are obtained, which are then utilized by the CFD solver in the next iteration of the computation.

Within each time step, the CFD and CSM solvers iterate until convergence is reached. Once the fluid and structural responses are consistent, the simulation advances to the next time step, where the coupling loop begins again.

In simple terms, the procedure can be viewed as a repeated exchange of information between the fluid and the structure. At each time step, the airflow loads deform the wing, and the deformed shape changes the airflow in return. This cycle continues until the interaction settles, after which the simulation advances to the next moment in time. In this way, the model captures how the wing and the surrounding air continuously influence one another during flapping.

To assess the need for turbulence modelling, we first note that the global Reynolds number lies in the laminar range (Re = 1,000–3,000), as also reported in experimental studies [5, 11]. However, due to the high flapping speed, the linear velocity near the wing tips locally reaches 5 m/s, yielding Reynolds numbers above 10^4. Therefore, additional analysis was performed on deformed geometries from FSI studies, with transient SBES (stress-blended eddy simulation) to capture these effects.

The computational domain included a parabolic velocity inlet, varying from 0 m/s at the symmetry plane to 5 m/s at the wing tip. The resulting aerodynamic forces closely match those obtained in FSI simulations that employed the RANS approach. In contrast, a purely laminar model substantially underestimates the forces (on average 35% lower in comparison to baseline) because it cannot adequately capture flow separation and partial reattachment at the wing tips (Fig. 4).

The mesh sensitivity studies were performed using the same set-up as in the turbulence model rationale. All meshes were prepared with $y+$ (non-dimensional wall distance) at the walls equal to 1 or less. The differences between them concerned the resolution in the flow separation region and the surface mesh density. The results are summarized in Table 2.

Using approximately 1 million elements yields the shortest reattachment length of 0.20 m and the lowest average force of 13.5 mN, indicating insufficient resolution of the separated shear layer. Increasing the mesh density to 3 million elements improves the predictions, extending the reattachment length to 0.32 m

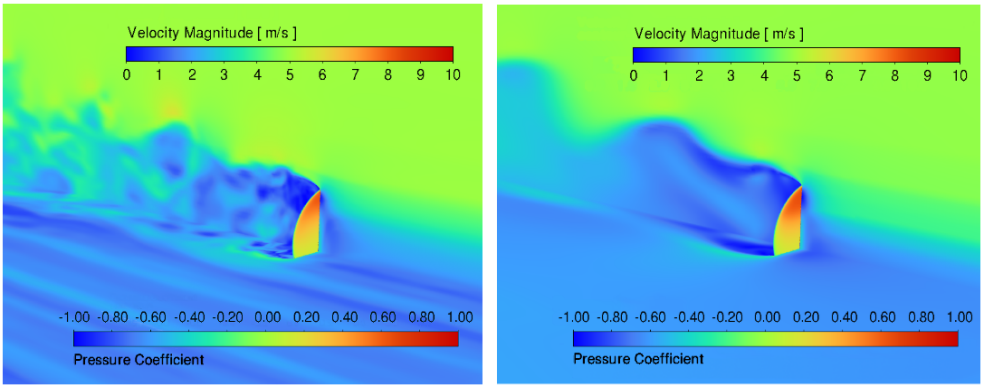

FIG. 4. Comparison of flow fields: SBES (left) and laminar steady RANS without a turbulence model (right). The figures display the velocity magnitude in the fluid domain and the pressure coefficient on the wing surface.

TABLE 2. Mesh sensitivity study: the lengths of flow reattachment and the obtained aerodynamic forces for various meshes tested.

Number of elements [–]	Length of flow reattachment [m]	Average force [mN]
1 mln	0.2	13.5
3 mln	0.32	14
11 mln	0.35	14.6

and increasing the mean force to 14 mN. The finest mesh, consisting of 11 million elements, produces a reattachment length of 0.35 m and an average force of 14.6 mN.

The gradual convergence of both quantities suggests that meshes above roughly 3 million elements capture the essential flow features with good accuracy, while the 11-million-element mesh provides only a moderate refinement benefit.

4. Numerical model

The numerical model consists of an overset mesh system (Fig. 5), with one mesh representing the moving wing and the other the stationary flow domain. The overset mesh technique, also known as Chimera grids [22], is commonly used to handle complex geometries and dynamic motions in CFD simulations. By employing a 'background' grid for the global domain and a body-fitted 'overset' grid for the vicinity of moving objects, it enables accurate flow resolution near dynamic boundaries, minimizes mesh distortion, and simplifies the simulation of large relative motions.

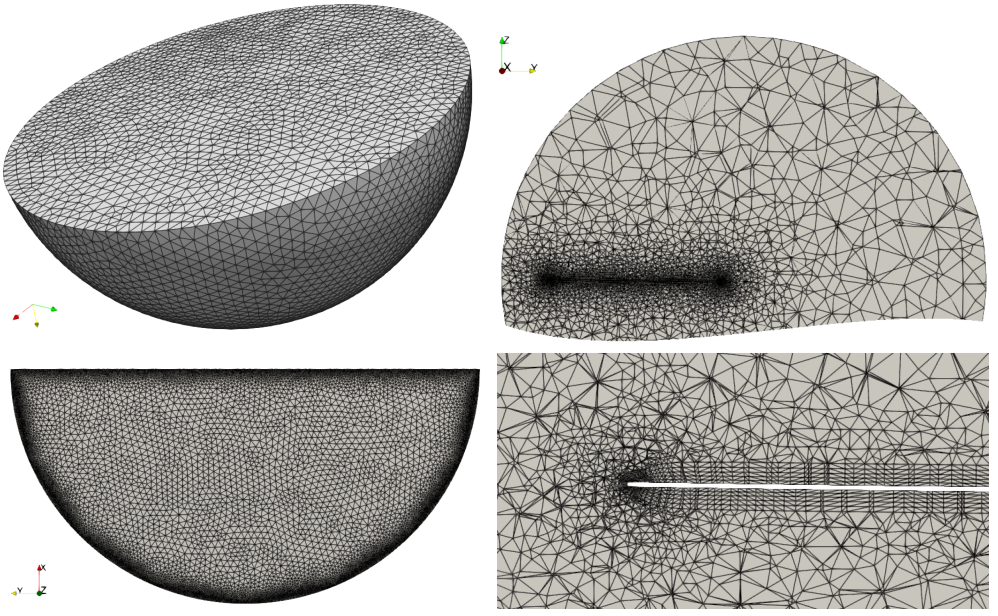

Fig. 5. The computational meshes used for aeroelastic simulations. Top-left: background, stationary mesh for far field. Top-right: section of overset mesh for moving region of fluid surrounding the wing. Bottom-right: detail of boundary layer in overset mesh. Bottom-left: surface mesh for the wing.

The mesh resolution was chosen to capture the details of the vortex dynamics around the flapping wing. The overset mesh consists of 3.19×10^5 nodes and 1.15×10^6 elements (with approximately 3.2×10^5 prisms forming a 5-layer boundary mesh with a growth rate of 1.1 and an initial layer thickness of 0.14 mm, and the remainder being tetrahedra), and a background mesh contains 4.17×10^4 tetrahedral elements and 8.24×10^2 nodes. There are 6.5×10^4 triangles and 3.3×10^4 nodes on the wing's surface mesh.

The boundary conditions for the fluid flow, modeled using the aforementioned RANS model, consisted of inlet/outlet conditions with zero velocity and atmospheric pressure of 101 325 Pa on spherical surfaces, a symmetry plane for the background mesh, an overset definition for the outer surface of the overset mesh, and a wall for the wing with motion coupled to the *Mechanical* solver.

The pressure-based transient solver employs cell-based spatial discretization using second-order upwind schemes. A SIMPLE (semi-implicit method for pressure linked equations) algorithm [23] is utilized for velocity-pressure coupling. The transient formulation is the first-order implicit, with a time step of 2.5×10^{-4} s, ensuring that the Courant–Friedrichs–Lewy (CFL) condition [24] is satisfied.

5. Results

5.1. Numerical analysis of flapping wing behavior

The first simulation presented was performed for a wing with membrane thickness of 0.15 mm and the flapping frequency equal to 30 Hz. The streamlines generated for the subsequent stages of the upstroke (when the wing moves in the positive Z direction), depicted in Fig. 6 visualize the vortices generated at the leading and trailing edges of the wing, that play a crucial role in force generation.

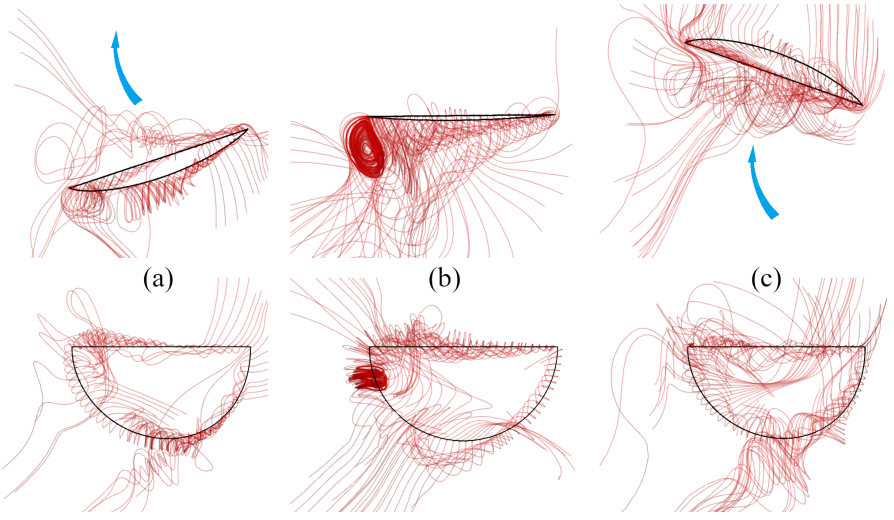

Fig. 6. The vortices generated on leading (straight) and trailing (curved) edges of the wing at subsequent stages of the upstroke. Top: YZ plane, bottom: YX plane (a) wing at the lowest position (start of upstroke), (b) wing in horizontal position (50% of upstroke), (c) wing at highest position (end of upstroke).

At the leading edge, leading-edge vortices (LEVs), generated mostly on the bottom side of the wing, enhance lift by creating a low-pressure region over the surface. This effect is illustrated in Fig. 7, where regions of low pressure can be observed on the upper side of the membrane near the leading edge, even in cases where the rest of the surface experiences overpressure. It should be noted that the pressure distribution shown in this figure has been limited using a color palette to values of ± 15 Pa relative to the ambient pressure. In reality, the pressures on the wing surfaces ranged from 101 249 to 101 357 Pa. The leading-edge vortices are visible for almost the entire stroke and they separate and vanish only at its end, when the wing reaches its extreme position.

The trailing-edge vortices have a similar effect on the pressure distribution, resulting in low pressure along all edges of the membrane at the beginning and

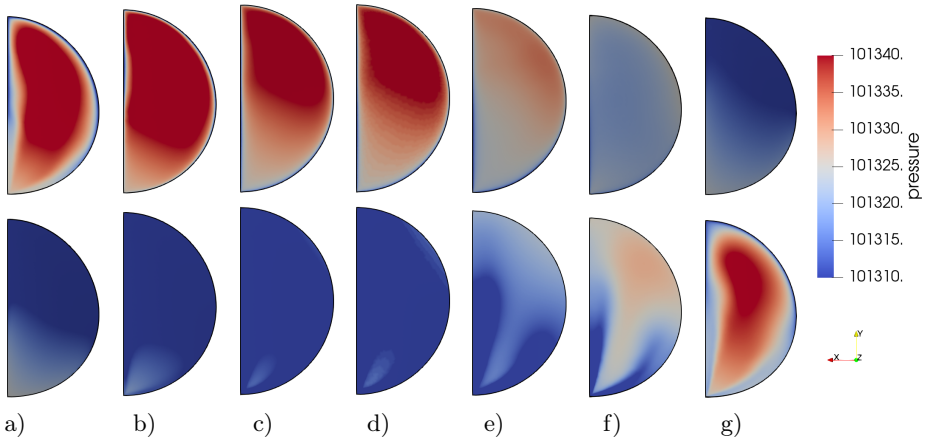

Fig. 7. The pressure distribution on top (positive z, top) and bottom (negative z) sides of the membrane for subsequent stages of the upstroke. The first (a), 0% of upstroke), the fourth (d), (50% of upstroke) and the last (g), 100% of upstroke) states counting from the left correspond to the ones depicted in Fig. 6).

end of the upstroke. In the middle of the upstroke, the separation of trailing-edge vortices from the wing increases the pressure in the middle and at the end (wingtip) of the bottom surface. This phenomenon, occurring at the end of the upstroke and the start of the downstroke, leads to a reversal of the pressure distributions on both sides of the membrane.

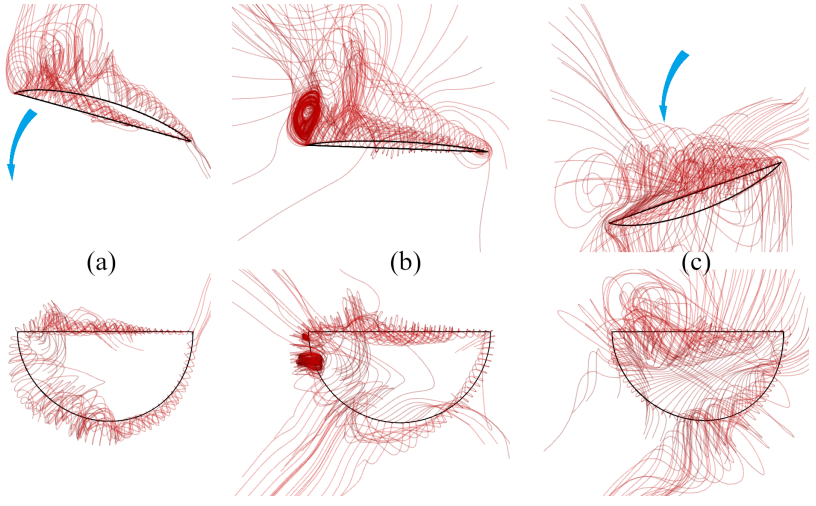

Fig. 8. The vortices generated on leading (straight) and trailing (curved) edges of the wing at subsequent stages of the downstroke. Top: YZ plane, bottom: YX plane; (a) wing at the highest position (start of downstroke), (b) wing in horizontal position (50% of downstroke), (c) wing at the lowest position (end of downstroke).

Regardless of the stroke phase, the streamlines run diagonally – opposite to both the X- and Z-axes, and aligned with the Y-axis. This is associated with the wing's flapping motion, which generates airflow from the leading edge to the trailing edge and outward, from the plane of symmetry toward the wingtip. As the wing moves up, it causes the airflow to move in the opposite direction (downward, as shown in the upper illustrations of Fig. 6).

During the downstroke (shown in Fig. 8), the arising phenomena are analogous. The leading-edge and trailing-edge vortices form above the wing, resulting in a pressure distribution opposite to that observed during the upstroke. In general, the upper surface experiences low pressure, while the lower surface experiences high pressure.

5.2. Effect of flapping frequency on thrust generation

The thrust and lift forces generated by a flapping wing with the same membrane thickness (0.15 mm) were analyzed across a range of flapping frequencies (10–30 Hz). The forces along the X- and Y-axes (drag/thrust and lift) were measured over time for 0.2 s of simulation, corresponding to two cycles at 10 Hz, three cycles at 15 Hz, and six cycles at 30 Hz, respectively. The results, related to the cycle phase and the displacement of a point at the midpoint of the leading edge, are shown on the left and right sides of Fig. 9.

The results indicate a clear trend of increasing average thrust and lift magnitudes with higher frequencies. For $f = 10$ Hz, the average thrust measured over the last cycles of flapping is 0.0468 mN, with values ranging from -0.0617 mN to 0.3654 mN. Meanwhile, the thrust reached a local (instantaneous) maximum value of 2.6641 mN at the beginning of the simulation, when the forces may not have fully converged. On the other hand, the lift, measured along the Y-axis, has a mean value of -0.4626 mN, and in the last cycles oscillates between -1.8026 mN and 0.5577 mN. This might be interpreted as the force acting towards the symmetry plane.

An increase in the flapping frequency leads to a corresponding increase in the average thrust generated by the wing (Fig. 10). The numerical results obtained for various flapping frequencies indicate that thrust generation is maximized at higher frequencies. For $f = 15$ Hz, the averaged thrust value is 0.1864 mN, four times larger than in the previous case. The maximum instantaneous thrust values are 0.7185 mN for the analyzed cycles and 4.8854 mN at the beginning of the simulation. A similar trend applies to the lift force: it reaches a mean value of -0.9927 mN and oscillates between -3.3589 mN and 0.7185 mN.

For this frequency and higher, the converged solutions allow the analysis of the relationship between aerodynamic forces and wing displacements. It can be observed that for zero displacement (neutral wing position), there is a small,

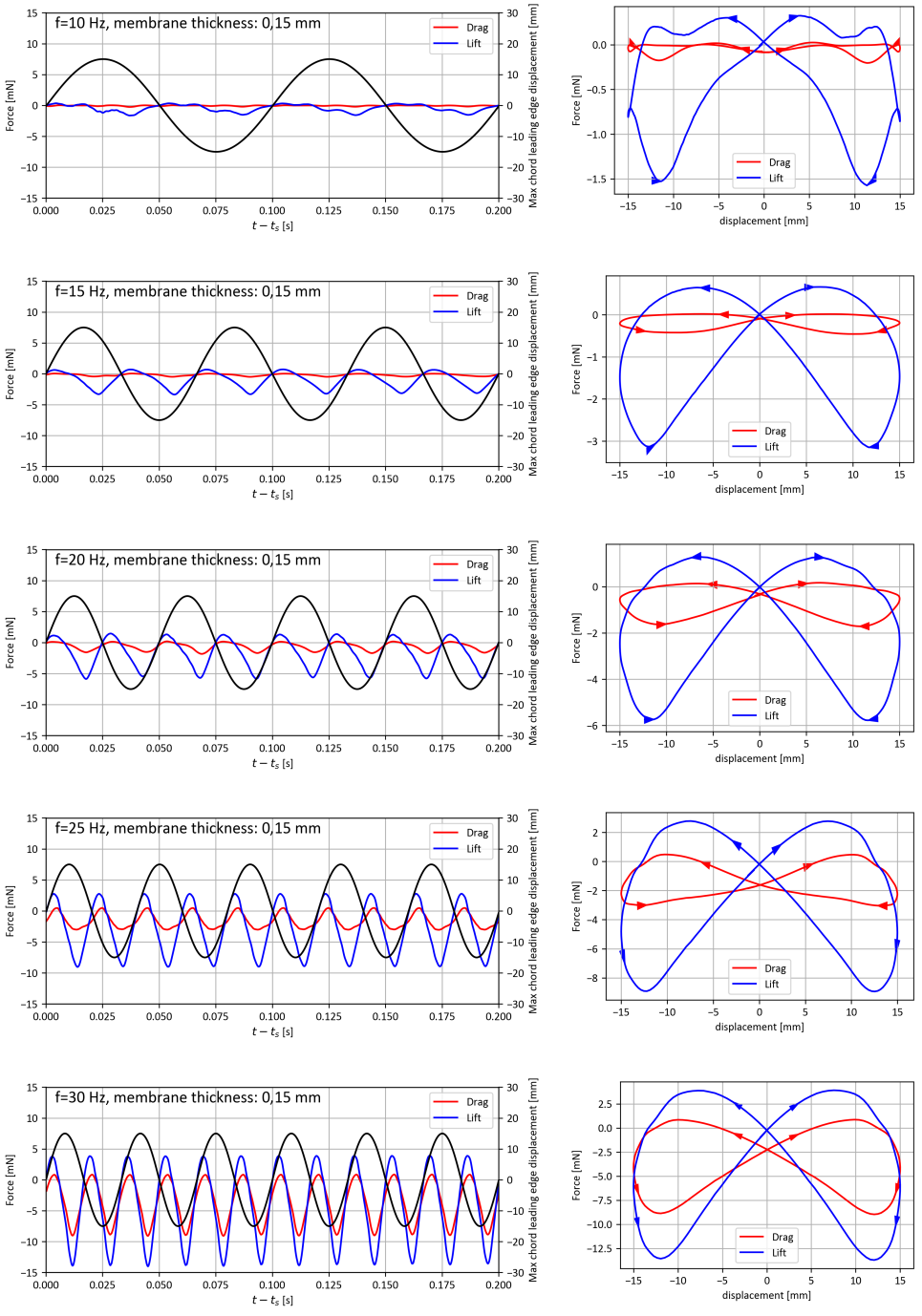

FIG. 9. Drag and lift as functions of time (left) and the displacements of the wing (right). The wing with a thickness of 0.15 mm at flapping frequencies, from top to bottom, of 10 Hz, 15 Hz, 20 Hz, 25 Hz, and 30 Hz.

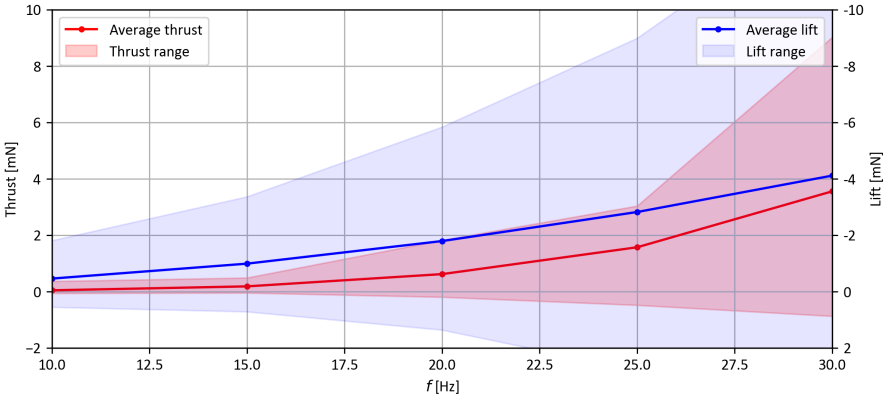

FIG. 10. Averaged drag and lift and their ranges as functions of frequency.

non-zero thrust that increases with the growth of the frequency. On the other hand, the instantaneous lift at zero displacement is zero. The largest thrust (negative drag) is observed when the displacement of the point at the middle of the leading edge is between 9 and 10 mm, after (where the maximum value is $A/2 = 15$ mm), shortly after the maximum displacement is reached. The moment of maximum thrust shifts towards the point of maximum displacement as the frequency increases. For $f = 25$ Hz and $f = 30$ Hz, the maximum thrust is observed at a displacement of approximately 12 mm out of a maximum of 15 mm. The corresponding time shift between the maximum displacement and maximum thrust is between 0.00325 s and 0.0035 s, which is approximately 1/10 of the flapping cycle.

Thrust and (negative) lift are in phase for flapping frequencies above 15 Hz.

For the highest analyzed frequency (30 Hz), the average thrust reached 3.5592 mN, with a peak value of 9.0267 mN. At the beginning of the flapping, the peak thrust observed was 13.9112 mN.

Similarly, the lift force exhibited negative averages at all frequencies, gradually decreasing to -4.1164 mN at $f = 30$ Hz, indicating stronger forces acting towards the symmetry plane at higher frequencies.

The increasing thrust – especially in relation to the slower increase in negative lift – indicates the relationship between the forces and the deformation of the membrane. Visualization of two points located at the middle of the leading edge and trailing edge, respectively (maximum chord position, Fig. 11), allows us to observe that with the increasing frequency of flapping, the deformation of the membrane along the chord becomes larger. The node located on the straight leading edge oscillates, as set in the boundary conditions, with a constant amplitude of 30 mm. On the other hand, the node located in the middle of the

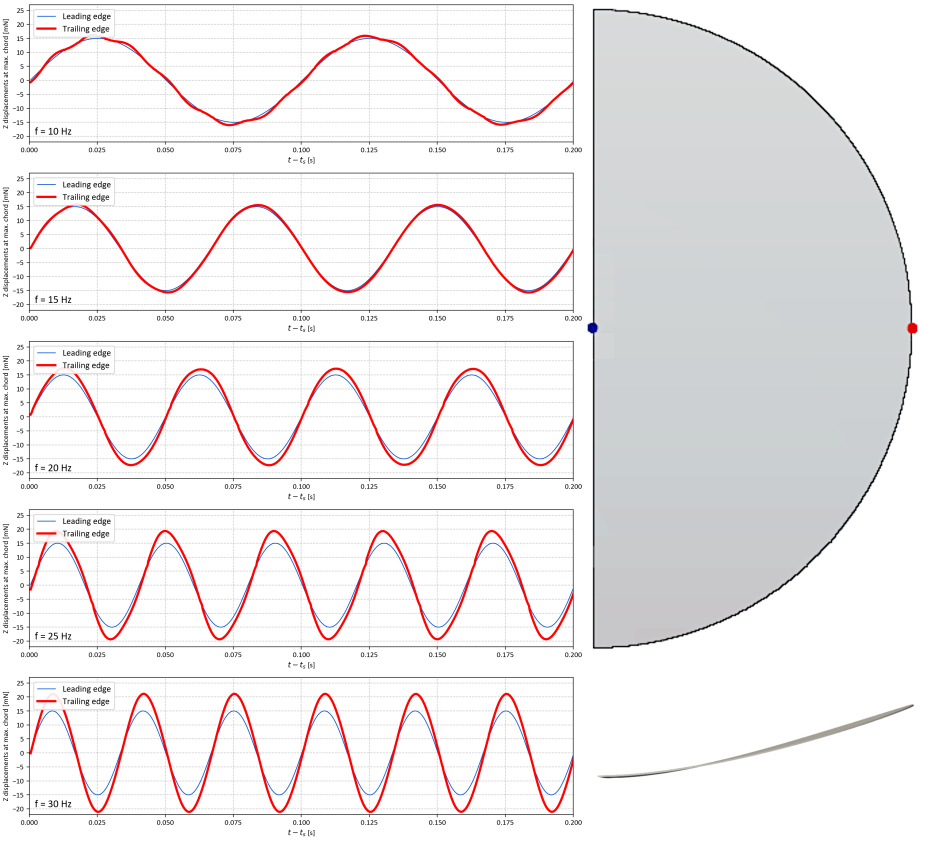

FIG. 11. Left: displacements in Z direction of nodes at maximum chord: leading vs. trailing edge. The wing with a thickness of 0.15 mm at flapping frequencies, from top to bottom, of 10 Hz, 15 Hz, 20 Hz, 25 Hz, and 30 Hz. Right: position of control points (top) and the maximum deflection of the 0.15 mm membrane for 30 Hz shown on a plane normal to the leading edge (bottom).

semicircle constituting the trailing edge oscillates with a slightly larger amplitude – the higher the flapping frequency, the larger the amplitude becomes. In the case of the frequency $f = 10$ Hz, the amplitudes of oscillation of both nodes are almost the same – resulting in the smallest generated thrust. For the frequency $f = 30$ Hz, displacements of a point lying on trailing edge are 1.408 times larger.

5.3. Effect of membrane thickness on thrust generation

The analysis of thrust and lift forces generated by membranes of varying thickness (0.15 mm, 0.25 mm, and 0.40 mm) at a constant flapping frequency of

30 Hz reveals key insights into the relationship between membrane deformation, stability, and aerodynamic performance The resulting forces are presented in Fig. 12, and the displacements for the last three cycles are depicted in Fig. 13.

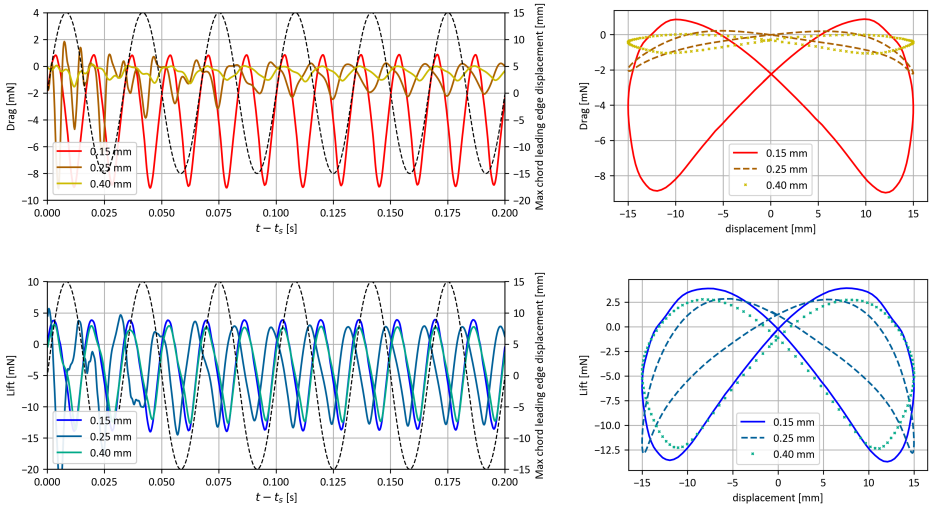

FIG. 12. Drag and lift as functions of time (left) and the displacements of the wing (right) for the thickness of the membrane equal to 0.15 mm, 0.25 mm and 0.40 mm, at flapping frequency of 30 Hz.

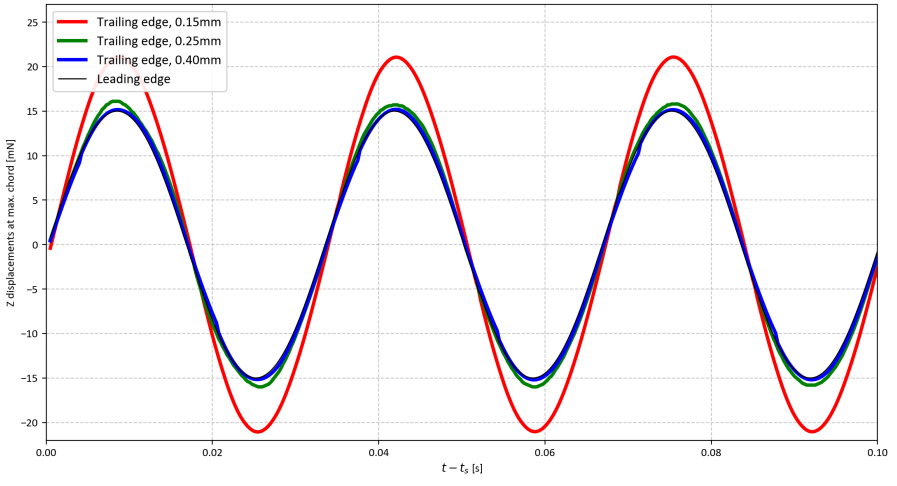

FIG. 13. Displacements in Z direction of nodes at maximum chord: leading vs. trailing edge for the thickness of the membrane equal to 0.15 mm, 0.25 mm and 0.40 mm, at flapping frequency of 30 Hz.

For thrust, the thinnest membrane (0.15 mm) achieves the highest average value of 3.5592 mN, with a wide range of values oscillating between −0.8725 mN and 9.0267 mN during the final cycles. The overall dataset shows extreme values between −5.9324 mN and 43.6019 mN, likely due to initial transient behavior. In comparison, the 0.25 mm membrane generates a lower average thrust of 0.8511 mN, with a narrower range of −0.2312 mN to 2.4677 mN during the last cycles. The maximum and minimum thrust values across the entire dataset are −3.4510 mN and 20.2585 mN, respectively. The thickest membrane (0.40 mm) produces the lowest average thrust of 0.4595 mN, with values oscillating between −0.0130 mN and 1.1483 mN during the final cycles and an overall range of −13.5343 mN to 11.2937 mN. In this case, oscillation amplitudes at corresponding points on the leading and trailing edges are similar. These results indicate that thicker membranes, thanks to their increased stiffness and smaller deformations, reduce thrust variability and enhance stability, albeit at the expense of aerodynamic efficiency.

In terms of lift, all membranes exhibit negative average values, indicating a consistent force directed toward the plane of symmetry. The 0.15 mm membrane has an average lift of −4.1164 mN, with oscillations ranging from −13.8336 mN to 3.9215 mN in the final cycles and extreme values in the dataset between −27.3713 mN and 13.9112 mN. The 0.25 mm membrane shows a similar average lift of −4.0095 mN, with a range of −13.3516 mN to 3.0286 mN during the last cycles and overall values between −29.3779 mN and 16.9391 mN. The 0.40 mm membrane exhibits an average lift of −3.9201 mN, oscillating between −12.4668 mN and 2.8401 mN in the final cycles and spanning a range of −25.1366 mN to 11.9393 mN across the dataset. These observations suggest that the lift remains relatively stable across different membrane thicknesses, with no clear trend of increasing or decreasing values. This consistency in lift values can be attributed to the same flapping amplitude, and the wing deformation resulting from its stiffness or thickness does not significantly influence this aerodynamic force component.

Overall, the results highlight a trade-off between aerodynamic performance and stability. As the membrane thickness is decreased (and its flexibility increased), wing deformations, particularly pitching of the trailing edge, became more pronounced. Thinner membranes generate higher thrust forces but are prone to greater variability, making them less stable. In contrast, thicker membranes exhibit improved stability but at the cost of reduced thrust. These findings emphasize the importance of selecting an appropriate membrane thickness based on the specific requirements of the application.

6. Summary

This study successfully simulates aeroelastic phenomena in flapping wings, providing detailed insights into the interplay between wing stiffness, flapping frequency, and aerodynamic forces. The numerical results support and extend the findings of Thiria and Godoy-Diana's experimental work [5], demonstrating a strong dependency of thrust generation on wing deformation, governed by membrane thickness and frequency of flapping.

The observed forces are noticeably smaller than those reported in the experiment, even when accounting for the symmetry assumptions in the numerical setup (a single wing versus a pair of wings in the experiment). A key difference lies in the treatment of the leading edge. In the simulation, the leading edge was modeled as perfectly rigid due to the applied boundary conditions. In contrast, in the experiment, it was reinforced with a fiberglass structure, whose material properties and stiffness were not explicitly defined. This likely enabled non-zero deformations not only in the chordwise direction but also along the leading edge itself, thereby enhancing the dynamic interaction between the wing structure and the surrounding airflow. Despite these differences, the trends in force generation, wing deformation, and vortex dynamics align well with the experimental observations, emphasizing the critical role of wing compliance in aerodynamic performance.

The presented method successfully captures the interactions between aerodynamic loads and structural deformations, enabling numerical modeling of wing behavior under varying flight conditions. By adjusting material distribution and stiffness across the wing, it is possible to balance aerodynamic efficiency and structural integrity. This capability provides a solid foundation for designing wing structures with an optimized elasticity profile, potentially leading to improved lift or thrust and enhanced performance in diverse flight scenarios.

Future directions include exploring additional parameters, such as varying airflow conditions and material properties (including potential nonlinearities), refining wing geometry for enhanced efficiency, and incorporating advanced turbulence modeling techniques. These findings contribute to the design of bio-inspired MAVs capable of efficient and stable flight in constrained environments.

Advances in micro-fabrication techniques provide a promising foundation for developing vein-like reinforcement structures that enable substantial membrane thinning without compromising mechanical integrity. By integrating micro-scale veins directly into the flexible substrate, the membrane achieves improved stiffness-to-weight characteristics while maintaining the structural integrity required for aerodynamic loading. This approach not only reduces overall mass but also enhances deformation control, making it highly suitable for applications such as bio-inspired MAV wings. Such developments offer strong prospects for manufac-

turing ultra-thin wings capable of withstanding higher actuation frequencies – conditions that have been shown in previous studies to increase thrust generation. Continued refinement of these fabrication processes will further expand design freedom, enabling more efficient, durable, and functionally graded membrane architectures.

Acknowledgments

The research was co-financed by the Polish National Agency for Academic Exchange (NAWA; grant no. BPN/BFR/2024/1/00020) and the Polish Ministry of Science and Higher Education (project no. 0612/SBAD/36280).

The authors acknowledge the collaboration with Université Polytechnique Hauts-de-France (UPHF) in the field of fluid-structure interaction within biomedical and bio-inspired micro-devices. The ideas and research directions presented in this article were partly inspired by ongoing joint activities, including academic exchanges and an internship undertaken by one of the authors at UPHF.

References

1. T. Hylton, C. Martin, R. Tun, V. Castelli, *The DARPA Nano Air Vehicle Program*, 50th AIAA Aerospace Sciences Meeting Including the New Horizons Forum and Aerospace Exposition, AIAA, 2012.
2. D. Faux, O. Thomas, E. Cattan, S. Grondel, *Two Modes resonant combined motion for insect wings kinematics reproduction and lift generation*, Europhysics Letters, **121**, 66001, 2018.
3. R.J. Wood, *Liftoff of a 60mg Flapping-Wing MAV*, 2007 IEEE/RSJ International Conference on Intelligent Robots and Systems, pp. 1889–1894, IEEE (Institute of Electrical and Electronics Engineers), 2007.
4. G.C.H.E. De Croon, M.A. Groen, C. De Wagter, B. Remes, R. Ruijsink, B.W. van Oudheusden, *Design, aerodynamics and autonomy of the DelFly*, Bioinspiration and Biomimetics, **7**, 2, 025003, 2012.
5. B. Thiria, R. Godoy-Diana, *How wing compliance drives the efficiency of self-propelled flapping flyers*, Physical Review E, **82**, 1, 015303, 2010.
6. S.P. Sane, *The aerodynamics of insect flight*, Journal of Experimental Biology, **206**, 23, 4191–4208, 2003.
7. K. Kawakami, S. Kaneko, G. Hong, H. Miyamoto, S. Yoshimura, *Fluid–structure interaction analysis of flexible flapping wing in the Martian environment*, Acta Astronautica, **193**, 138–151, 2022.
8. B. Gupta, E. Sihite, A. Ramezani, *Modeling and controls of fluid–structure interactions (FSI) in dynamic morphing flight*, 2024, https://arxiv.org/abs/2406.13039 (preprint).
9. D. Drikakis, D. Fung, I.W. Kokkinakis, S.M. Spottswood, K.R. Brouwer, Z.B. Riley, D. Daub, A. Gülhan, *High-speed fluid–structure Interaction predictions using a deep learning transformer architecture*, Physics of Fluids, **37**, 5, 2025.

10. A. TIBA, T. DAIRAY, F. DE VUYST, I. MORTAZAVI, J.-P. BERRO RAMIREZ, *Machine-learning enhanced predictors for accelerated convergence of partitioned fluid–structure interaction simulations*, Computer Physics Communications, **310**, 109522, 2025.

11. S. RAMANANARIVO, R. GODOY-DIANA, B. THIRIA, *Rather than tesonance, flapping wing flyers may play on aerodynamics to improve performance*, Proceedings of the National Academy of Sciences, **108**, 15, 5964–5969, 2011.

12. S.A. COMBES, T.L. DANIEL, *Flexural stiffness in insect wings I. Scaling and the influence of wing venation*, Journal of Experimental Biology, **206**, 17, 2979–2987, 2003.

13. R. ROSZAK, P. POSADZY, W. STANKIEWICZ, M. MORZYŃSKI, *Fluid–structure interaction for large scale complex geometry and non-linear properties of structure*, Archives of Mechanics, **61**, 1, 3–27, 2009.

14. J. DONEA, A. HUERTA, J-PH. PONTHOT, A. RODRÍGUEZ-FERRAN, *Arbitrary Lagrangian–Eulerian Methods*, Encyclopedia of Computational Mechanics, 2004.

15. C. FARHAT, C. DEGAND, B. KOOBUS, M. LESOINNE, *Torsional springs for two-dimensional dynamic unstructured fluid meshes*, Computer Methods in Applied Mechanics and Engineering, **163**, 1-4, 231–245, 1998.

16. D.K. WALTERS, D. COKLJAT, *A three-equation eddy–viscosity model for Reynolds-averaged Navier–Stokes simulations of transitional flow*, Journal of Fluids Engineering, **130**, 121401, 2008.

17. D.C. WILCOX, *Simulation of transition with a two-equation turbulence model*, AIAA (American Institute of Aeronautics and Astronautics) Journal, **32**, 2, 247–255, 1994.

18. S.K. CHIMAKURTHI, S. REUSS, M. TOOLEY, S. SCAMPOLI, *ANSYS Workbench system coupling: a state-of-the-art computational framework for analyzing multiphysics problems*, Engneering with Computers, **34**, 385–411, 2018.

19. K. KOTECKI, H. HAUSA, M. NOWAK, W. STANKIEWICZ, R. ROSZAK, M. MORZYŃSKI, *Deformation of Curvilinear Meshes for Aeroelastic Analysis*, IDIHOM: Industrialization of High-Order Methods – A Top-Down Approach, pp. 125–131, Springer, 2015.

20. K. JANSEN, F. SHAKIB, T. HUGHES, *Fast projection algorithm for unstructured meshes*, [in:] Computational Nonlinear Mechanics in Aerospace Engineering (A93-12151 02-31), 1992.

21. F. BOS, *Numerical Simulation of Flapping Foil and Wind Aerodynamics: Mesh Deformation Using Radial Basis Functions*, PhD thesis, TU Delft, 2009.

22. U. BURGGRAF, M. KUNTZ, B. SCHÖNING, *Implementation of the Chimera Method in the Unstructured DLR Finite Volume Code TAU*, New Results in Numerical and Experimental Fluid Mechanics II: Contributions to the 11th AG STAB/DGLR Symposium, pp. 93–100, Springer, 1999.

23. S. PATANKAR, *Numerical Heat Transfer and Fluid Flow*, CRC Press, 2018.

24. R. COURANT, K. FRIEDRICHS, H. LEWY, *Über die partiellen Differenzengleichungen der mathematischen Physik*, Mathematische Annalen, **100**, 1, 32–74, 1928.

Received March 4, 2025; revised version December 18, 2025.
Published online January 28, 2026.